BMC Medical Imaging

RESEARCH Open Access

# Radiomics application using non-contrast computed tomography for predicting uric acid kidney stones

Yang Huang[1,2], Ning Li[2], Xiaowei Han[3], Shufeng Xu[3], Guozheng Zhang[3,4*] and Xisong Zhu[3*]

## Abstract

**Objective** This study aims to develop a prediction model based on non-contrast computed tomography (NCCT) images to differentiate uric acid stones from non-uric acid stones before treatment.

**Methods** This study retrospectively enrolled 195 patients from Quzhou People's Hospital between 2022 and 2024 who underwent dual-energy CT scans with confirmed renal stone composition. The patients were randomly divided into a training set (156 cases) and a test set (39 cases) in an 8:2 ratio. Regions of interest (ROIs) were manually delineated slice-by-slice on NCCT images to extract radiomic features. Feature dimensionality reduction and selection were performed using intraclass correlation coefficient (ICC), Spearman rank correlation coefficients, and least absolute shrinkage and selection operator (LASSO) regression. Radiomics and clinical models were developed using logistic regression (LR), support vector machine (SVM), multilayer perceptron (MLP), ExtraTrees, and LightGBM algorithms. Finally, a combined model was constructed by integrating the selected radiomic features with clinically significant risk factors. Model performance was evaluated using the area under the receiver operating characteristic curve (AUC), while clinical utility was assessed through decision curve analysis (DCA). Model interpretability was examined using Shapley additive explanations (SHAP).

**Results** A total of 1834 radiomic features were extracted from each ROI. After feature dimensionality reduction and selection, 6 radiomic features remained for characterizing stone composition. The clinical, radiomics, and combined models all demonstrated favorable discriminatory power for uric acid stones. The AUC values of the three models in the training set were 0.744 (95% CI: 0.666–0.822), 0.831 (95% CI: 0.766–0.897), and 0.886 (95% CI: 0.834–0.938), respectively, and 0.778 (95% CI: 0.631–0.925), 0.634 (95% CI: 0.454–0.777), and 0.805 (95% CI: 0.666–0.944) in the test set. DeLong's test indicated that in the training set, the performance of the combined model was significantly superior to both the clinical model and the radiomics model (0.886 vs. 0.744, $p < 0.001$; 0.886 vs. 0.831, $p = 0.015$). Decision curve analysis also demonstrated its potential clinical utility. SHAP analysis revealed that texture features were important factors in predicting uric acid stones.

*Correspondence:
Guozheng Zhang
zgz_0007@163.com
Xisong Zhu
zhuxisong@126.com

Full list of author information is available at the end of the article

**Conclusion** The combined model based on NCCT performs well in distinguishing uric acid stones and can provide effective references for treatment decisions.

**Clinical trial number** Not applicable.

**Keywords** Radiomics, Uric acid stones, Stone composition analysis, Dual-energy CT

## Introduction

Urolithiasis is a global disease with high incidence and recurrence rates. The main components of stones include uric acid, cystine, calcium oxalate, etc., with uric acid stones accounting for 10–15% of all urolithiasis cases [1–3]. Knowing the stone composition before treatment is clinically significant for selecting the most appropriate treatment method and preventing recurrence. The treatment approach for uric acid (UA) stones differs from other types of stones; clinically, they can be dissolved through urine alkalinization, thereby avoiding complications such as renal hemorrhage and secondary hypertension caused by extracorporeal shock wave lithotripsy to a certain extent [4, 5]. Furthermore, UA stones can reveal underlying metabolic abnormalities, allowing for specific medications or dietary restrictions to be implemented to prevent recurrence [6, 7]. Therefore, identifying whether a stone is composed of urate before treatment is particularly important.

Computed tomography (CT) is a commonly used non-invasive imaging technique for detecting uric acid stones, but its ability to differentiate stone compositions is limited. According to the 2015 gout classification criteria established by the American College of Rheumatology (ACR) and the European League Against Rheumatism (EULAR), dual-energy CT is one of the effective and precise methods for identifying the composition of uric acid stones [8]. Dual-energy computed tomography (DECT) operates on the principle of material decomposition, enabling non-invasive compositional discrimination by analyzing the differential attenuation characteristics of stones at different X-ray energy levels. Studies have demonstrated its high diagnostic accuracy for in vivo identification of uric acid stones, with both sensitivity and specificity exceeding 90–95% [9], Its efficacy has been extensively validated and shows strong agreement with ex vivo infrared spectroscopy [10]. As a non-invasive in vivo diagnostic technique, DECT can provide reliable stone composition information without the need for surgical intervention. Consequently, it has been recommended as a reference standard for preoperative stone characterization by authoritative guidelines such as those of the European Association of Urology [8]. However, dual-energy CT equipment is expensive, and the examination costs are high, making it not yet widely available. Therefore, developing a model based on non-contrast-enhanced CT (NCCT) for identifying uric acid stones has significant clinical application value.

Radiomics is an emerging image analysis technique whose radiomic features can reflect the underlying pathophysiological processes of diseases. These features can be used to construct predictive models, thereby supporting clinical decision-making processes such as disease diagnosis, prognostic evaluation, and treatment efficacy monitoring [11, 12]. Currently, radiomics is applied in the differentiation of uric acid stone compositions, prognostic evaluation, and complication assessment [13–15]. However, previous studies have mainly relied on postoperative spectral analysis as the gold standard, meaning that patients with uric acid stones also had to undergo traumatic surgical treatment. Additionally, some past research has primarily focused on texture features [16, 17], neglecting the potential value of clinical data and radiomic features. Therefore, this study aims to establish a combined model based on NCCT radiomic features and clinical features, using dual-energy CT as the gold standard for diagnosing urate composition [8], to better assist in the formulation of clinical diagnosis and treatment decisions.

## Materials and methods

### Patient data

Quzhou People's Hospital review board approved this retrospective study. We retrospectively collected data from 351 patients who underwent dual-energy CT (DECT) and had their kidney stone compositions confirmed via the PACS system at Quzhou People's Hospital from 2021 to 2024 (Table 1).

Inclusion criteria were as follows: (a) patients who underwent abdominal non-contrast CT for non-urolithiasis conditions and had a non-contrast dual-energy CT (DECT) scan within six months before or after that confirmed renal stone composition; (b) availability of complete imaging and clinical data; (c) for patients with multiple stones, one stone was selected; (d) if stone compositions differed, uric acid stones were prioritized; (e) if all stones had the same composition, the stone with the longest maximum diameter ($>5$ mm) was selected. Exclusion criteria included: (a) stones too small for accurate delineation; (b) poor CT image quality or significant artifacts; (c) concomitant other urinary tract diseases such as tumors or malformations.Baseline clinical data—including age, sex, weight, height, uric acid level,

**Table 1** Patient information of enrolled participants

| Characteristics | Training set | | | | Test set | | | |
|---|---|---|---|---|---|---|---|---|
| | ALL | Non-urinary stone | urinary stone | *P Value* | ALL | Non-urinary stone | urinary stone | *P Value* |
| Age | 50.19±14.42 | 48.79±14.86 | 52.09±13.67 | 0.158 | 52.36±15.38 | 52.14±16.27 | 52.65±14.63 | 0.920 |
| Gender | | | | | | | | |
| Male | 139(89.10%) | 80(88.89%) | 59(89.39%) | 1.000 | 4(10.26%) | 2(9.09%) | 2(11.76%) | 1.000 |
| Female | 17(10.90%) | 10(11.11%) | 7(10.61%) | 1.000 | 35(89.74%) | 20(90.91%) | 15(88.24%) | 1.000 |
| Diameter | 0.50±0.41 | 0.44±0.34 | 0.58±0.48 | 0.013 | 0.49±0.39 | 0.47±0.38 | 0.52±0.41 | 0.655 |
| CT_L | 168.63±106.43 | 171.24±117.72 | 165.06±89.52 | 0.964 | 188.38±189.82 | 210.82±246.68 | 159.35±64.18 | |
| CT_H | 712.03±428.75 | 810.63±436.91 | 577.56±380.99 | <0.001 | 755.67±385.76 | 920.23±376.97 | 542.71±285.46 | 0.002 |
| CT_Avg | 428.40±236.60 | 485.94±237.67 | 349.95±212.88 | <0.001 | 461.77±247.06 | 556.43±263.19 | 339.26±160.59 | 0.007 |
| Blood uric acid | 405.79±130.61 | 415.07±142.52 | 393.14±112.19 | 0.302 | 394.39±110.15 | 378.37±108.39 | 415.11±112.19 | 0.308 |
| Urine creatinine | 9761.54±4927.49 | 9366.28±4479.03 | 10300.52±5469.78 | 0.183 | 8575.31±4179.13 | 9044.19±5143.10 | 7968.52±2463.45 | 0.776 |
| Serum creatinine | 90.73±40.41 | 88.46±35.69 | 93.84±46.19 | 0.910 | 99.03±45.55 | 97.17±46.46 | 101.44±45.65 | 0.620 |
| Urinary leukocytes | 624.39±5090.54 | 1023.02±6684.54 | 80.81±303.96 | 0.183 | 9.91±19.57 | 5.97±7.39 | 15.01±28.08 | 0.450 |
| Urinary albumin to creatinine ratio | 155.63±357.17 | 114.48±189.14 | 211.73±499.68 | 0.489 | 111.98±271.55 | 83.30±98.79 | 149.10±399.67 | 0.313 |
| CRP | 55.17±28.46 | 54.83±28.29 | 55.62±28.90 | 0.989 | 59.79±30.45 | 61.80±25.83 | 57.18±36.24 | 0.645 |

urinary creatinine, serum creatinine, presence of bilateral or unilateral stones, and stone location—were obtained from medical records. To ensure stone stability between NCCT and DECT scans, we further excluded cases where any stone-related treatment (e.g., ESWL, URS, PCNL) was performed between the two scans, or where imaging indicated spontaneous stone passage. All included stones were confirmed to be in the same anatomical location in both scans.A total of 195 stones from 195 patients were included. Based on DECT analysis, stone compositions included uric acid, calcium oxalate, calcium phosphate, cystine, etc. These were categorized into uric acid (UA, n = 83) and non-uric acid (nUA, $n = 112$) groups. The cases were randomly divided into training and test sets in an 8:2 ratio, with 65 UA stones in the training set and 18 in the test set. A flowchart detailing participant inclusion/exclusion is provided in Fig. 1, The detailed workflow is illustrated in Fig. 2.

### CT image acquisition

Dual-Energy CT Parameters:

Toshiba Aquilion one TSX-301C 320-slice dual-energy CT was used, with high and low tube voltages of 135kV and 80kV, respectively, an original tube current of 200mAs, CareDoes4D, a matrix of 512 × 512, a collimator of 0.5 × 320, a reconstructed slice thickness of 1 mm, a slice interval of 1 mm, and a tube rotation time of 0.5s.

Non-Contrast CT Parameters:

Siemens SOMATOM Definition AS 64-slice CT was used, with a tube voltage of 120kV, an original tube current of 200mAs, CareDoes4D, a matrix of 512 × 512, a collimator of 0.625 × 64, a reconstructed slice thickness of 1 mm, a slice interval of 1 mm, and a tube rotation time of 0.5s.

### Parameters for stone classification using dual-energy CT

All dual-energy CT (DECT) images were analyzed on a dedicated post-processing workstation (Toshiba Aquilion One TSX-301C/320). Stone composition was differentiated based on predetermined attenuation slope ratios of known stone types: uric acid, calcium oxalate, and cystine exhibit slope values of 1.06, 0.74, and 0.80, respectively. Since different stone materials exhibit distinct CT attenuation values at 135 kV and 85 kV, an unknown stone generates a specific data point in the attenuation coordinate system. Its composition is determined by comparing its slope against the reference values of known stone types.

### Construction of clinical model

First, a baseline analysis of clinical data was conducted to compare the clinical characteristics between the training and validation sets. Then, a comprehensive analysis of clinical data—including patient demographics and imaging features—was performed. Based on this analysis and a review of relevant literature, clinical risk factors were identified. Finally, a clinical prediction model was constructed.

### Stone segmentation and feature extraction

A radiologist with three years of experience in abdominal imaging used ITK-SNAP software (Version 3.6.0, http://www.itksnap.org/) to delineate the region of interest (ROI) layer by layer. The ROI was drawn along the edge

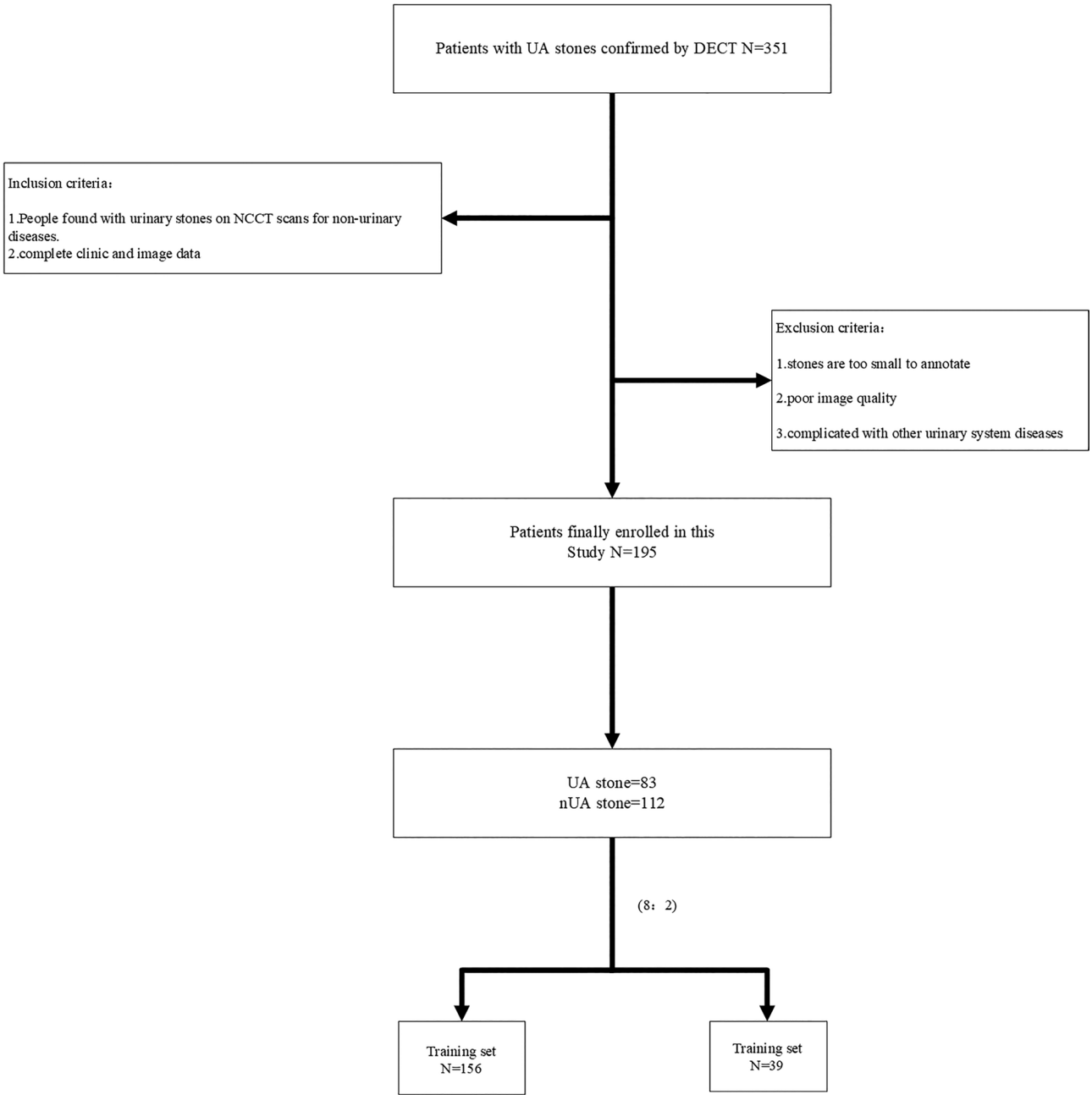


**Fig. 1** Patient enrollment flowchart. Patient enrollment process and detailed inclusion and exclusion criteria

of the stone, avoiding surrounding renal tissue, vessels, fat, or image artifacts as much as possible.

First, image preprocessing was performed by resampling all images to a uniform voxel size of 1 mm × 1 mm × 1 mm using linear interpolation. Then, gray-level discretization was applied with a bin width of 25 to convert continuous image values into discrete integer values. Finally, logarithmic and wavelet image filters were used to remove mixed noise introduced during image digitization and to extract high- or low-frequency features.An open-source software, PyRadiomics version 2.2.0 (https://github.com/Radiomics/pyradiomics), was used to extract radiomic features from the stones. These features can be categorized into four groups: (a) shape features, (b) first-order statistical features, (c) texture features, and (d) higher-order texture features.

### Inter and intra observer consistency

To assess inter-observer consistency, we used the intra-class correlation coefficient (ICC). A radiologist with three years of abdominal imaging experience (HY) randomly selected 40 patients and delineated the ROIs. One

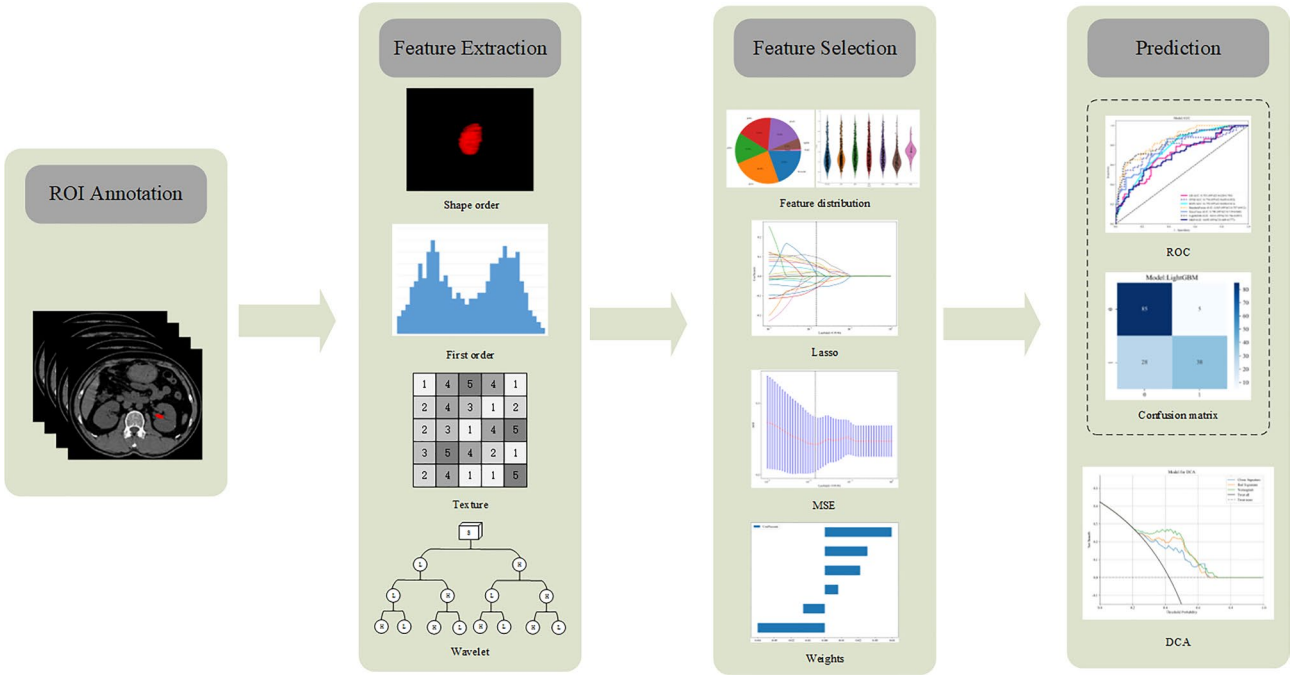


**Fig. 2** Detailed radiomics workflow. The specific process of radiomics for predicting stone composition: manual segmentation of the stone; feature extraction and reduction; model establishment; and stone composition prediction

week later, another radiologist with 15 years of abdominal imaging experience independently re-delineated the ROIs for these 40 patients and extracted the corresponding radiomic features. We considered an ICC value above 0.75 as satisfactory for feature extraction reproducibility.

### Radiomics feature selection and model construction

We performed high-throughput radiomic feature extraction on CT images and randomly divided the dataset into training and test sets in an 8:2 ratio. Multiple rounds of feature dimensionality reduction were then applied to the radiomic features within the training set. Intra- and inter-observer reliability was assessed using the intraclass correlation coefficient (ICC). Redundant features were filtered using the Pearson correlation coefficient, whereby if the correlation coefficient between any two features exceeded 0.9, only one of them was retained. Subsequently, the most relevant features were selected using the Least Absolute Shrinkage and Selection Operator (LASSO) method to develop the radiomics model. The overall workflow is illustrated in Fig. 3.

Based on the previously selected radiomic signature (Rad_signature), machine learning algorithms including logistic regression (LR), support vector machine (SVM), multilayer perceptron (MLP), ExtraTrees, and LightGBM were employed to construct the radiomics models. After building the models using the training dataset, their performance was evaluated on the test dataset. Receiver operating characteristic (ROC) curves were plotted, and evaluation metrics such as the area under the ROC curve (AUC), sensitivity, specificity, and accuracy were calculated.

### Interpretability of the radiomics model

SHapley Additive exPlanations (SHAP) values were used to calculate the distribution of features in the prediction model [18]. To enhance model interpretability, the SHAP method was employed to explain the constructed machine learning models, addressing the "black box" issue of the models. All analyses were conducted using the SHAP library (version 2.0.0) in the Python environment, and SHAP summary plots were generated. To visualize the contribution of each feature to the final outcome, representative cases were selected to create SHAP Force plots (Fig. 5).

### Construction of the combined model

Clinical factors such as age, gender, weight, height, uric acid, urinary creatinine, serum creatinine, stone composition, bilateral or unilateral kidney stones, stone location, stone CT value, and maximum stone diameter on CT were analyzed through univariate and multivariate analyses to screen for clinically independent risk factors. These factors were then combined with the best machine learning model to construct the combined model.

### Clinical application

In the validation cohort, decision curve analysis (DCA) was used to compare the clinical model, radiomic model, and combined model by evaluating clinical performance

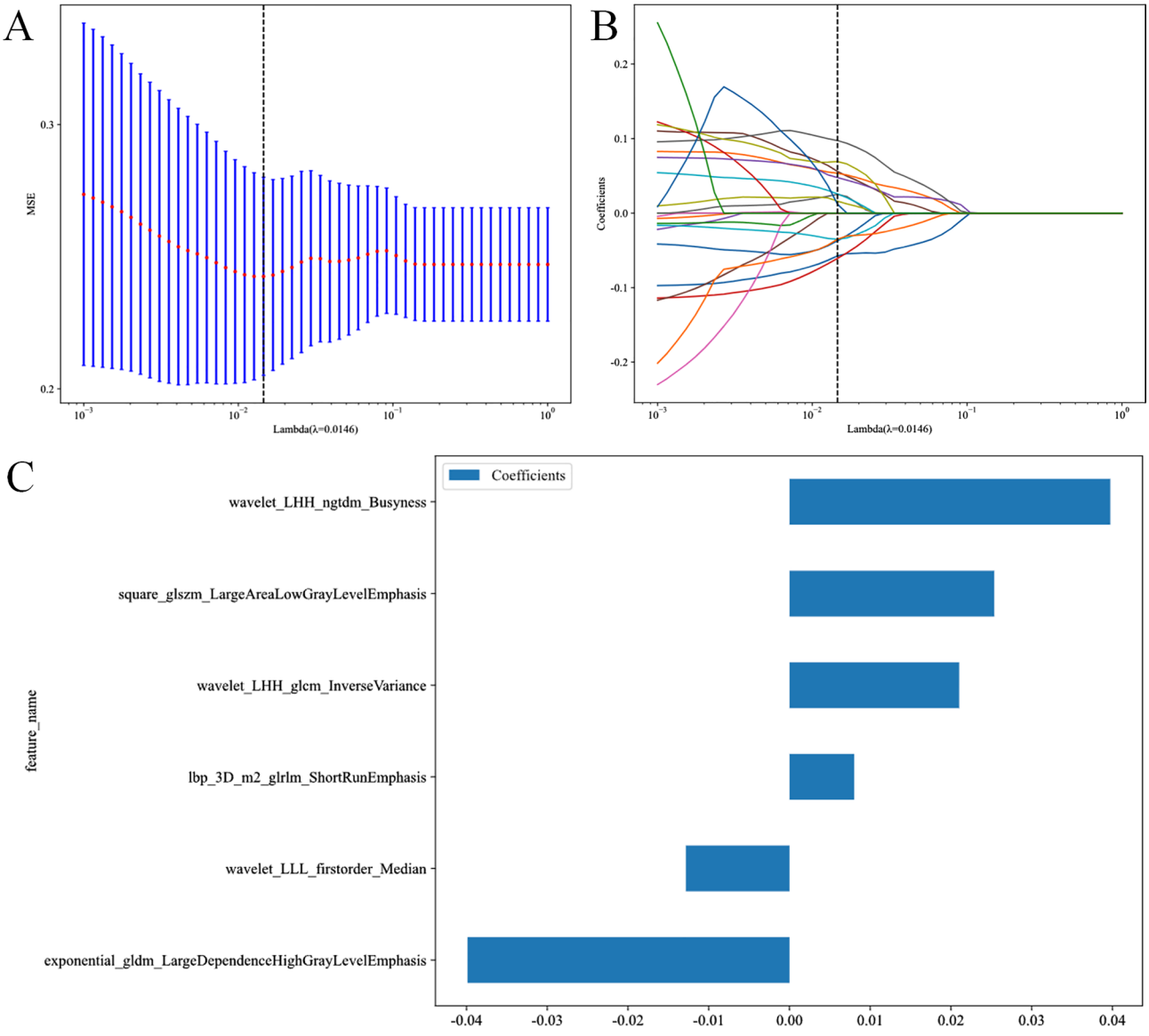


**Fig. 3** Radiomics feature selection based on LASSO and Establishment of rad-signature. Using LASSO regression for radiomics feature selection. **A**: the optimal λ value of 0.015. **B**: the LASSO coefficient profiles for the 6 radiomics features were plotted against the selected log(λ) value, utilizing five-fold cross validation. **C**: the radiomics features with non-zero coefficients were selected, along with their corresponding coefficients

at different threshold probabilities. The goal was to determine which model provided the greatest net benefit in predicting stone composition.

### Statistical analysis

Continuous variables were compared using independent t-tests or Mann-Whitney U tests for intergroup differences, while categorical variables were assessed using chi-square tests. Receiver operating characteristic (ROC) curves were employed to evaluate the performance of each model, and DeLong's test was used to compare the differences between models. To assess the clinical usefulness of the nomogram, decision curve analysis (DCA) was performed by calculating the net benefit across a range of threshold probabilities in the entire cohort. A p-value < 0.05 was considered statistically significant.

## Results

### Clinical data analysis

This study analyzed 195 patients with comprehensive clinical and imaging data collected. Table 1 provides a detailed comparison of clinical and imaging factors between uric acid stones and non-uric acid stones in the training and validation sets. The training set consisted of 156 patients (139 males and 17 females), including 66 classified as uric acid stones and 90 as non-uric acid stones. The validation set comprised 39 patients (4 males and 35 females), with 17 classified as uric acid stones and

**Table 2** Univariate and multivariate analysis of clinical features

| Variables | Univariate logistic regression | | Multiple-stepwise logistic regression analysis | |
|---|---|---|---|---|
| | OR (95%CI) | P-value | OR (95%CI) | P-value |
| Gender | 0.737(0.556-0.978) | 0.076 | - | - |
| Diameter | 0.636(1.436-0.857) | 0.857 | - | - |
| Age | 0.996(0.990-1.001) | 0.145 | - | - |
| CRP | 0.996(0.991-1.000) | 0.104 | - | - |
| Serum_creatinine | 0.998(0.995-1.000) | .0156 | - | - |
| CT_L | 0.999(0.997-1.000) | 0.074 | - | - |
| CT_H | 0.999(0.999-1.000) | 0.001 | 1.001(0.997-1.004) | 0.384 |
| CT_ave | 0.999(0.998-0.999) | 0.001 | 0.997(0.991-1.003) | 0.690 |
| Blood_uric_acid | 0.999(0.999-1.000) | 0.033 | 1.001(1.000-1.002) | 0.221 |
| Urine_creatinine | 1.000(1.000-1.000) | 0.234 | - | - |
| Urinary_leukocytes | 1.000(1.000-1.000) | 0.431 | - | - |
| Urinary_albumin_to_creatinine_ratio | 1.000(1.000-1.001) | 0.463 | -- | - |

OR: Odds Ratio, CI: Confidence Interval

22 as non-uric acid stones. Analysis of clinical baseline data revealed significant differences in Diameter, CT_H, and CT_ave within the training set ($P < 0.05$).

Univariate and multivariate logistic regression analyses did not identify any independent clinical risk factors (Table 2). Based on previous literature and clinical data analysis, CT_H, CT_ave, and Blood_uric_acid were selected for constructing the clinical prediction model. The model achieved an AUC of 0.744 (95% CI: 0.666–0.822) in the training set and an AUC of 0.778 (95% CI: 0.631–0.925) in the validation set.

### Radiomic feature extraction

A total of 1834 radiomic features were extracted from each ROI，A total of 1563 features remained following ICC screening.After screening using the Pearson correlation coefficient, 25 features remained. Subsequently, Least Absolute Shrinkage and Selection Operator (LASSO) regression was used for further feature selection, leaving 6 features to establish the radiomic model. The flowchart is shown in Fig. 4.

The Rad-signature is calculated using the following formula:

Rad_signature=0.4230769230769231
-0.039878*exponential_gldm_
LargeDependenceHighGrayLevelEmphasis
+0.008011*lbp_3D_m2_glrlm_ShortRunEmphasis
+0.025358*square_glszm_
LargeAreaLowGrayLevelEmphasis
+0.021019*wavelet_LHH_glcm_InverseVariance
+0.039738*wavelet_LHH_ngtdm_Busyness
-0.012840*wavelet_LLL_firstorder_Median

### Construction and comparison of different radiomic models

This study employed logistic regression (LR), support vector machine (SVM), multilayer perceptron (MLP), ExtraTrees, and LightGBM to develop radiomics-based prediction models, with the results summarized in Table 3. LightGBM demonstrated the highest area under the curve (AUC) values in both the training and test sets,

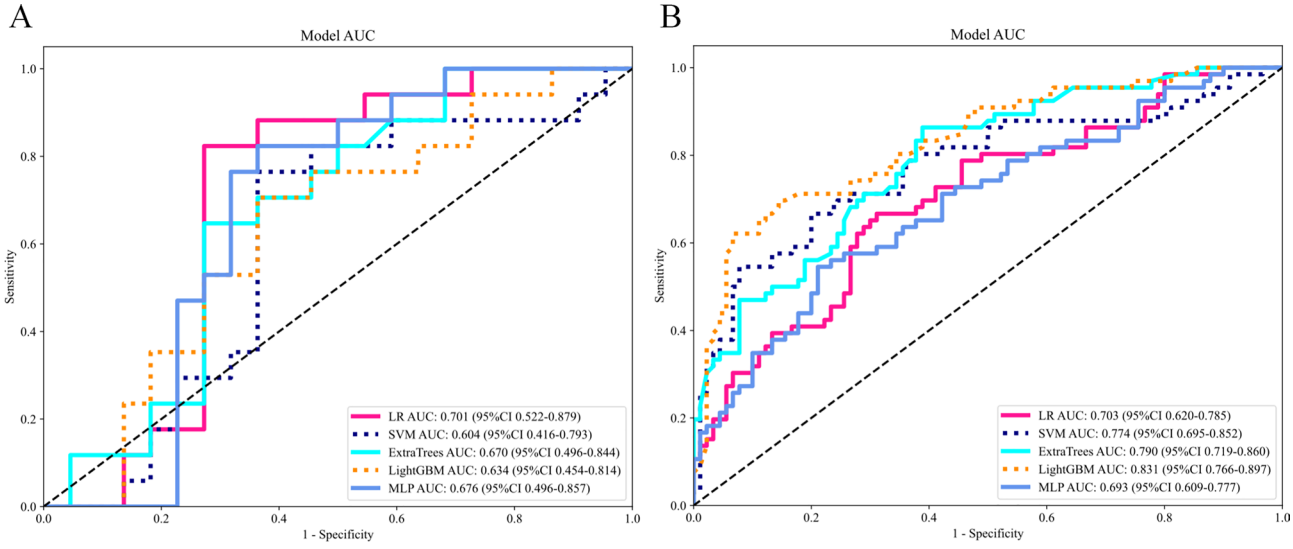


**Fig. 4** Comparison of AUC values for various radiomics models on training (**A**) and test (**B**) sets. LR: Logistic Regression; SVM: support vector machine; ET: extraTrees; LightGBM: light gradient boosting machine; MLP: multilayer perceptron; AUC: the area under the receiver operating characteristic curve

**Table 3** Comparison of the performance of various radiomics models

| | AUC | Precision | Specificity | F1-Score |
|---|---|---|---|---|
| Training set | | | | |
| LR | 0.703(0.620-0.785) | 0.606 | 0.689 | 0.628 |
| SVM | 0.774(0.695-0.852) | 0.833 | 0.922 | 0.648 |
| ET | 0.790(0.719-0.860) | 0.615 | 0.611 | 0.713 |
| LightGBM | 0.831(0.766-0.897) | 0.870 | 0.933 | 0.714 |
| MLP | 0.693(0.609-0.857) | 0.648 | 0.789 | 0.583 |
| Test set | | | | |
| LR | 0.701(0.522-0.879) | 0.684 | 0.727 | 0.722 |
| SVM | 0.604(0.416-0.793) | 0.600 | 0.636 | 0.649 |
| ET | 0.670(0.496-0.844) | 0.625 | 0.727 | 0.606 |
| LightGBM | 0.634(0.454-0.777) | 0.579 | 0.636 | 0.611 |
| MLP | 0.676(0.496-0.857) | 0.619 | 0.636 | 0.684 |

LR: Logistic Regression; SVM: Support Vector Machine; ET: extraTrees; LightGBM: Light Gradient Boosting Machine; MLP: Multilayer Perceptron; AUC: the area under the receiver operating characteristic curve

achieving AUCs of 0.831 (95% CI: 0.766–0.897) and 0.634 (95% CI: 0.454–0.777), respectively.

#### Interpretability of the radiomic model

We calculated the SHAP values for each radiomic feature in the LightGBM model (Fig. 5). The results demonstrated that square_glszm_LargeAreaLowGrayLevelEmphasis, wavelet_LHH_glcm_InverseVariance, and wavelet_LHH_ngtdm_Busyness exhibited strong correlations with uric acid stones.

#### Construction and evaluation of the combined clinical-radiomic model

By integrating clinical features with radiomic features, the combined model using the LightGBM algorithm achieved the best performance, with AUCs of 0.886 (95% CI 0.834–0.938) for the training set and 0.805 (95% CI 0.666–0.944) for the test set (Fig. 6). To compare the differences between models, the Delong test was used. The results showed that, in the training set, the combined model significantly outperformed both the clinical model and the radiomic model (0.886 vs. 0.744, $P < 0.001$; 0.886 vs. 0.831, $P = 0.015$) (Table 4).

#### Decision curve analysis (DCA) comparison of clinical, radiomic, and combined models, and clinical application of the nomogram

In this study, we also evaluated each model using DCA (Fig. 7). Compared to scenarios without any predictive model intervention (i.e., all treatment or no treatment), the clinical model, radiomic model, and combined model significantly improved patient intervention outcomes, with the combined model providing the greatest benefit. Preoperative imaging was effective in predicting whether the stones were urate. Figure 7 presents the nomogram based on clinical features and radiomic features.

## Discussion

Development and Validation of a Radiomics Nomogram for Preoperative Non-Invasive Prediction of Uric Acid Stones Based on NCCT.

This study developed a radiomics nomogram model by integrating NCCT-based radiomic features and clinical indicators for the non-invasive preoperative prediction of uric acid stones. The results demonstrate that the model exhibits favorable predictive performance and may provide valuable reference for clinical decision-making.

Accurate preoperative prediction of uric acid stone composition is critical for formulating individualized treatment plans. In recent years, radiomics analysis has offered a novel approach for non-invasive discrimination of stone composition. Kaviani et al. constructed a stone composition prediction model based on threshold segmentation and radiomics, reporting an AUC of 0.78 [19]. Zheng et al. conducted a multicenter study to develop and validate a non-invasive radiological model using machine learning for in vivo identification of infection stones, thereby optimizing the management of urolithiasis and significantly improving patient outcomes [20]. However, most of these studies relied on postoperative ex vivo stone analysis as the gold standard, which is invasive. In contrast, our study used dual-energy CT (DECT) as the reference standard, enabling non-invasive prediction before treatment, thus offering greater clinical practicality.All DECT images were analyzed on a dedicated post-processing workstation (Toshiba Aquilion One TSX-301C/320). The core principle of stone composition discrimination with this system lies in the differential CT attenuation of stones at 135 kV and 85 kV energy levels. By calculating the attenuation slope and comparing it with reference values of known compositions (e.g., approximately 1.06 for uric acid, 0.74 for calcium oxalate, and 0.80 for cystine), the composition of unknown stones can be determined. We further constructed a combined predictive model by integrating clinical indicators and radiomic features. Previous studies have indicated associations between stone CT values, blood uric acid levels, and stone composition [21–23], which is consistent with our findings.

This study identified significant differences in CT attenuation values between uric acid and non-uric acid stones, likely attributable to the distinct physicochemical properties of uric acid stones. Uric acid stones originate from the end product of purine metabolism, their formation is highly dependent on urinary pH, and their crystalline structure is relatively loose with micro-gaps, resulting in generally lower CT values [24, 25]. This finding provides a theoretical basis for non-invasive discrimination. In constructing our predictive model, variable selection was guided by both statistical and clinical considerations. Although CT_H and CT_ave did not both

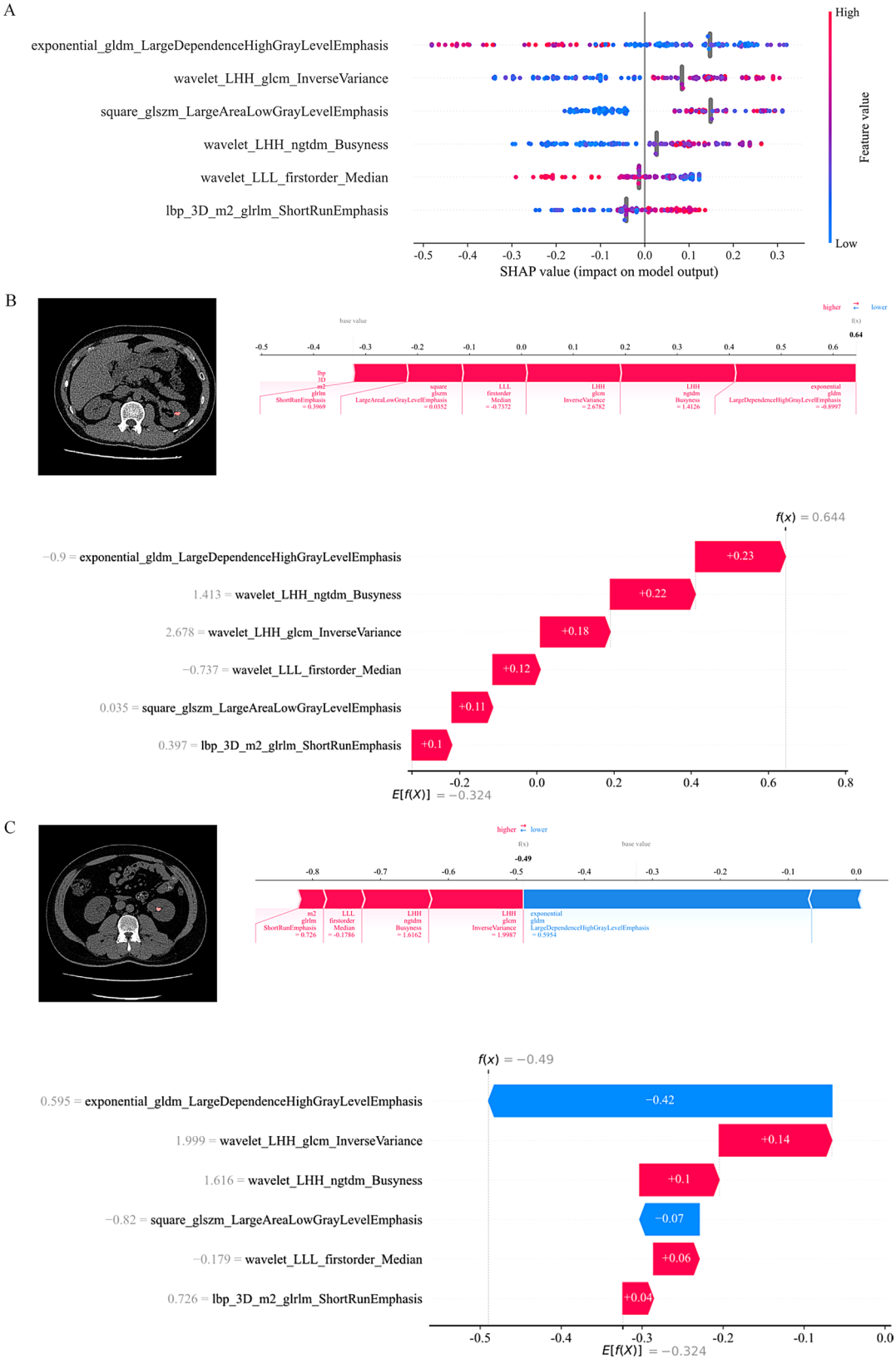


**Fig. 5** SHAP analysis of Radiomics feature weights. (**A**): feature inspection; two representative cases correctly predicted as uric acid stone (**B**) and non-uric acid stone (**C**) were individually visualized by SHAP method. SHAP, Shapley additive explanation

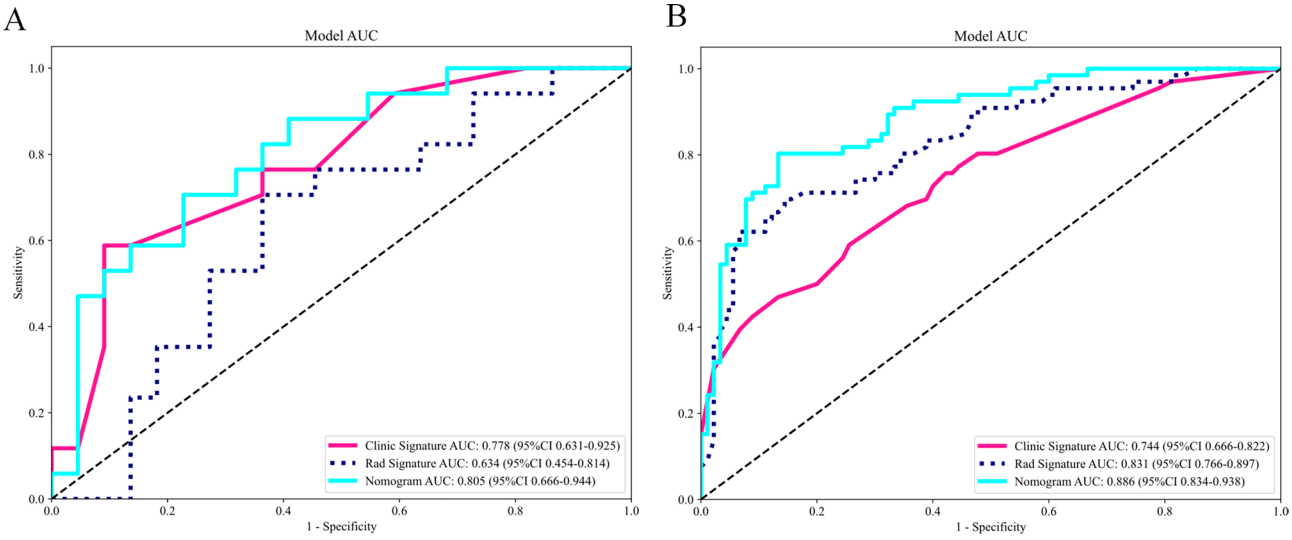


**Fig. 6** Comparison of AUC values for clinical models, radiomics models, and nomogram on training (**A**) and test (**B**) sets. The nomogram demonstrated excellent performance on both the training set and the test set

**Table 4** Comparison of the performance of clinical models, radiomics models, and nomogram

| | AUC | Precision | Specificity | F1-Score |
|---|---|---|---|---|
| Training set | | | | |
| Clinic | 0.744(0.666-0.822) | 0.778 | 0.911 | 0.579 |
| Radiomics | 0.831(0.766-0.897) | 0.870 | 0.933 | 0.714 |
| Nomogram | 0.886(0.834-0.938) | 0.812 | 0.867 | 0.800 |
| Test set | | | | |
| Clinic | 0.778(0.631-0.925) | 0.818 | 0.909 | 0.643 |
| Radiomics | 0.634(0.454-0.814) | 0.579 | 0.636 | 0.611 |
| Nomogram | 0.805(0.666-0.944) | 0.687 | 0.773 | 0.667 |

retain statistical significance in multivariate analysis due to multicollinearity, we included both—along with blood uric acid—in the final model based on the well-established role of CT values in stone composition discrimination and the key pathophysiological role of blood uric acid in uric acid stone formation [9, 26]. The final model demonstrated good discriminatory performance in the validation set, supporting the practicality of this clinically-informed variable selection strategy.

Through feature selection, we identified six radiomic features with the highest predictive value, five of which were texture features and one first-order feature. These features effectively reflect intra-stone heterogeneity and microstructural information. Notably, texture features (e.g., exponential_gldm_LargeDependenceHighGrayLevelEmphasis) reflect the spatial distribution of pixel gray levels, potentially corresponding to the characteristic porous structure of uric acid stones [27–29]. First-order features (e.g., wavelet_LLL_firstorder_Median) describe the overall distribution of gray-level intensities [30, 31]. The combination of these features provides comprehensive imaging basis for accurate identification of uric acid stones. Specifically, the selected texture features—square_glszm_LargeAreaLowGrayLevelEmphasis, wavelet_LHH_glcm_InverseVariance, and wavelet_LHH_ngtdm_Busyness—may reflect two critical characteristics of uric acid stones on CT imaging: internal homogeneity and relatively low density. These features offer quantitative metrics from the perspectives of overall density distribution, local uniformity, and boundary clarity, collectively forming robust imaging markers for identifying uric acid stones.

We compared the performance of five machine learning algorithms and ultimately selected the LightGBM algorithm for integrated modeling due to its advantages in computational efficiency and resistance to overfitting when handling high-dimensional feature data [32]. The combined model based on radiomics and clinical features achieved an AUC of 0.805 (95% CI: 0.666–0.944) in the test set, demonstrating good discriminatory ability. Decision curve analysis (DCA) further indicated that the nomogram provides clinical net benefit across a wide range of threshold probabilities, supporting its potential practical value.

Our study has several limitations. First, the patients were recruited from a single center, and the generalizability of the model requires validation with multicenter data. Second, although manual segmentation is considered the gold standard, it is time-consuming and labor-intensive. Future studies could explore fully automatic segmentation methods to reduce manual effort. Third, this study employed traditional machine learning methods and did not incorporate advanced deep learning algorithms, which warrants further investigation. Additionally, in cases of multiple stones, we applied the "one patient, one stone" principle to ensure data

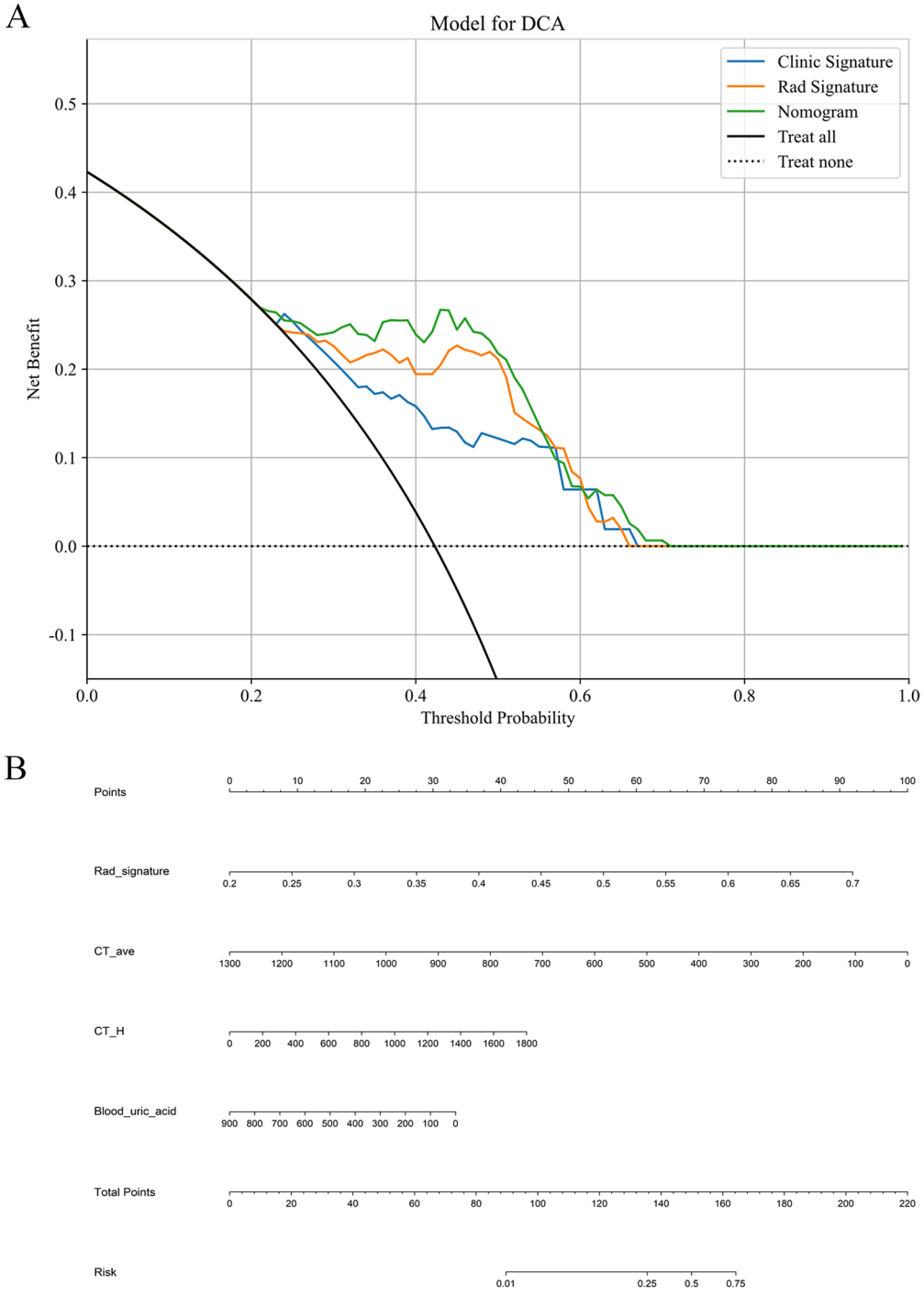


**Fig. 7** Comparison of DCA for clinical models, radiomics models, and nomogram on training and test Sets (**A**) and clinical application of the nomogram (**B**). A decision curve analysis (DCA) of the clinical models, radiomics models, and nomogram. B the radiomics features combined with CT_AVG,CT_H, and blood uric acid to establish a CT-based nomogram. The DCA indicates that within the majority of threshold probabilities, the use of the nomogram yielded greater net benefit

independence, which may overlook heterogeneity among stones within the same patient. Future research could explore more complex models capable of handling such clustered data.

## Conclusion

In summary, this study developed and validated a preoperative prediction method for identifying urate stone composition based on a nomogram that combines radiomics and clinical features derived from NCCT.

It provides an effective, non-invasive, and convenient method for optimizing disease management and precision medicine for patients with kidney stones and their doctors.

**Acknowledgements**
I would like to thank Dr. Xisong Zhu for providing the means and encouragement to write and publish this paper. At the same time, I am particularly grateful to thank Dr. Guozheng Zhang for providing technical support, completing the data processing section, and participating in the revision of the paper. In addition, it is necessary to thank Dr. Shufeng Xu for his help and encouragement in writing. I would like to express my gratitude to Dr. Xiaowei Han for helping me clarify and answer my questions in pathology.

**Author contributions**
Research Concept and Design: Yang Huang, Xiaowei Han, Guozheng Zhang Shufeng Xu; Data collection and analysis: Yang Huang, Ning Li; Writing and Revision: Yang Huang, Xiaowei Han, Guozheng Zhang, Xisong Zhu; Statistical expertise and other support: Xiaowei Han, Guozheng Zhang All authors have given their approval to the final manuscript and acknowledge their responsibility for every aspect of the work, committing to thoroughly address and resolve any inquiries concerning the accuracy or integrity of any portion of the research.

**Funding**
This work was supported by Quzhou Science and Technology Bureau project (2022k65), and Research Fund of Quzhou Science and Technology Bureau(2020FK03).

**Data availability**
The original contributions presented in the study are included in the article. Further inquiries can be directed to the corresponding author.

## Declarations

**Ethics approval and consent to participate**
The research including clinical images received ethical approval for from the Ethics Committee of the Quzhou People's Hospital. All research procedures were carried out in accordance with the Declaration of Helsinki (2000) of the World Medical Association.and the informed consent form was signed by the patients or their families.

**Consent of publication**
Not applicable.

**Conflicts of interests**
The authors declare no competing interests.

**Author details**
[1]Department of Radiology, The Fourth Affiliated Hospital of School of Medicine, and International School of Medicine, International Institutes of Medicine, Zhejiang University, Yiwu 322000, China
[2]Zhejiang Chinese Medical University, Hangzhou 310053, China
[3]Department of Radiology, Wenzhou Medical University Affiliated Quzhou Hospital (Quzhou People's Hospital), Quzhou 324000, China
[4]Department of Quzhou Key Laboratory of Respiratory Mechanics in Critical Care Medicine, Wenzhou Medical University Affiliated Quzhou Hospital (Quzhou People's Hospital), Quzhou 324000, China

Received: 21 November 2024 / Accepted: 24 September 2025
Published online: 29 October 2025

**References**

1. Skolarikos A, Somani B, Neisius A, et al. Metabolic evaluation and recurrence prevention for urinary stone patients: an EAU guidelines update. Eur Urol. 2024;86(4):343–63.
2. Türk C, Petřík A, Sarica K, et al. EAU guidelines on interventional treatment for urolithiasis. Eur Urol. 2016;69(3):475–82.
3. Türk C, Petřík A, Sarica K, et al. EAU guidelines on diagnosis and conservative management of urolithiasis. Eur Urol. 2016;69(3):468–74.
4. Wang Y, Lu J. The management of diabetes with Hyperuricemia: can we hit two birds with one stone. J Inflamm Res. 2023;16:6431–41.
5. Adomako E, Moe OW. Uric acid and urate in urolithiasis: the innocent bystander, instigator, and perpetrator. Semin Nephrol. 2020;40(6):564–73.
6. Jou YC, Fang CY, Chen SY, et al. Proteomic study of renal uric acid stone. Urology. 2012;80(2):260–66.
7. Maiuolo J, Oppedisano F, Gratteri S, Muscoli C, Mollace V. Regulation of uric acid metabolism and excretion. Int J Cardiol. 2016;213:8–14.
8. Neogi T, Jansen TL, Dalbeth N, et al. Gout classification criteria: an American college of rheumatology/European league against rheumatism collaborative initiative. Ann Rheum Dis. 2015;74(10):1789–98.
9. Primak AN, Fletcher JG, Vrtiska TJ, et al. Noninvasive differentiation of uric acid versus non-uric acid kidney stones using dual-energy CT. Acad Radiol. 2007;14(12):1441–47.
10. Hidas G, Eliahou R, Duvdevani M, et al. Determination of renal stone composition with dual-energy CT: in vivo analysis and comparison with x-ray diffraction. Radiology. 2010;257(2):394–401.
11. Akinci D'Antonoli, Cuocolo R, Baessler B, Pinto Dos Santos D. Towards reproducible radiomics research: introduction of a database for radiomics studies. Eur Radiol. 2024;34(1):436–43.
12. Guiot J, Vaidyanathan A, Deprez L, et al. A review in radiomics: making personalized medicine a reality via routine imaging. Med Res Rev. 2022;42(1):426–40.
13. Nakamae Y, Deguchi R, Nemoto M, et al. AI prediction of extracorporeal shock wave lithotripsy outcomes for ureteral stones by machine learning-based analysis with a variety of stone and patient characteristics. Urolithiasis. 2023;52(1):9.
14. Xun Y, Li J, Geng Y, et al. Single extracorporeal shock-wave lithotripsy for proximal ureter stones: can CT texture analysis technique help predict the therapeutic effect. Eur J Radiol. 2018;107:84–89.
15. Wang R, Su Y, Mao C, Li S, You M, Xiang S. Laser lithotripsy for proximal ureteral calculi in adults: can 3D CT texture analysis help predict treatment success. Eur Radiol. 2021;31(6):3734–44.
16. Mannil M, von Spiczak J, Hermanns T, Poyet C, Alkadhi H, Fankhauser CD. Three-dimensional texture analysis with machine learning provides incremental predictive information for successful shock wave lithotripsy in patients with kidney stones. J Urol. 2018;200(4):829–36.
17. Zhang GM, Sun H, Shi B, Xu M, Xue HD, Jin ZY. Uric acid versus non-uric acid urinary stones: differentiation with single energy CT texture analysis. Clin Radiol. 2018;73(9):792–99.
18. Ejiyi CJ, Cai D, Ejiyi MB, et al. Polynomial-SHAP analysis of liver disease markers for capturing of complex feature interactions in machine learning models. Comput Biol Med. 2024;182:109168.
19. Kaviani P, Primak A, Bizzo B, et al. Performance of threshold-based stone segmentation and radiomics for determining the composition of kidney stones from single-energy CT. Jpn J Radiol. 2023;41(2):194–200.
20. Zheng J, Yu H, Batur J, et al. A multicenter study to develop a non-invasive radiomic model to identify urinary infection stone in vivo using machine-learning. Kidney Int. 2021;100(4):870–80.
21. Zheng J, Zhang J, Cai J, et al. Development of a radiomics model to discriminate ammonium uric acid stones from uric acid stones in vivo: a remedy for the diagnostic pitfall of dual-energy computed tomography. Chin Med J (engl). 2024;137(9):1095–104.
22. Jin L, Chen Z, Sun Y, Tian Z, Yi X, Huang Y. Advancements in uric acid stone detection: Integrating deep learning with CT imaging and clinical assessments in the upper urinary tract. Urol Int. 2024;108(3):234–41.
23. Tran TY, Bamberger JN, Blum KA, et al. Predicting the impacted ureteral stone with computed tomography. Urology. 2019;130:43–47.
24. Pourvaziri A, Parakh A, Cao J, et al. Comparison of four dual-energy CT scanner technologies for determining renal stone composition: a phantom approach. Radiology. 2022;304(3):580–89.
25. Molloy R, Sun W, Chen J, Zhou W. Structure and cleavage of monosodium urate monohydrate crystals. Chem Commun (camb). 2019;55(15):2178–81.
26. Wan KS, Liu CK, Ko MC, Lee WK, Huang CS. Nephrolithiasis among male patients with newly diagnosed gout. Hong Kong Med J. 2016;22(6):534–37.
27. Stępień M, Chrzan R, Gawlas W. In vitro analysis of urinary stone composition in dual-energy computed tomography. Pol J Radiol. 2018;83:e421–25.

28. Xu Z, Li M, Li B, Shu H. Synthesis of virtual monoenergetic images from kilovoltage peak images using wavelet loss enhanced CycleGAN for improving radiomics features reproducibility. Quant Imag Med Surg. 2024;14(3):2370–90.
29. Corrias G, Micheletti G, Barberini L, Suri JS, Saba L. Texture analysis imaging "what a clinical radiologist needs to know". Eur J Radiol. 2022;146:110055.
30. Tang VH, Duong S, Nguyen C, et al. Wavelet radiomics features from multiphase CT images for screening hepatocellular carcinoma: analysis and comparison. Sci Rep. 2023;13(1):19559.
31. Jiang Z, Yin J, Han P, et al. Wavelet transformation can enhance computed tomography texture features: a multicenter radiomics study for grade assessment of COVID-19 pulmonary lesions. Quant Imag Med Surg. 2022;12(10):4758–70.
32. Yanagawa R, Iwadoh K, Akabane M, et al. LightGBM outperforms other machine learning techniques in predicting graft failure after liver transplantation: creation of a predictive model through large-scale analysis. Clin transplant. 2024;38(4):e15316.

## Publisher's Note